Energy gain in collisions of highly charged ions with C_{60}

U. Thumm,[1] A. Bárány,[2] H. Cederquist,[2] L. Hägg,[2] and C. J. Setterlind[2]

[1]*John R. Macdonald Laboratory, Department of Physics, Kansas State University, Manhattan, Kansas 66506-2604*
[2]*Atomic Physics, Stockholm University, Frescativägen 24, S-104 05 Stockholm, Sweden*

We have extended the recently developed dynamical classical over-barrier model for charge transfer in soft ion-cluster collisions in order to simulate the projectile kinetic energy gain of $3.3q$-keV Ar^{q+} ions in large-impact-parameter collisions with neutral C_{60} targets. Our semiclassical theory allows for the direct calculation of the energy defect Q and of the projectile kinetic-energy gain in two different ways: either as difference of electronic binding energies before and after the collision or by integration of the dynamically varying force between the collision partners along the trajectory. A comparison between the two ways provides an intrinsic test of the model calculations. A comparison with recent experimental data shows good agreement in the main features of the projectile energy gain spectra and facilitates their interpretation in terms of the number of transferred electrons and projectile shells into which electrons are captured. [S1050-2947(97)04512-5]

PACS number(s): 34.50.Bw, 34.70.+e, 82.30.Fi, 61.46.+w

I. INTRODUCTION

Since the invention of a method for producing macroscopic amounts of fullerenes [1], an increasing number of experiments have probed the collisional interactions of these symmetric and stable carbon clusters [2]. Lately, a few groups have started to use both fast [3] and slow [4–7] highly charged ions as projectiles. Typical processes studied have been fragmentation, ionization, and charge transfer. At low collision energy the dominating primary processes are single- and multiple-electron transfer. The latter process often leads to the secondary process of electron emission. For large-impact-parameter (soft) collisions, fragmentation of the recoiling C_{60} ions is relatively unimportant even when several electrons have been removed [5]. In this paper we focus on a different simulation of the projectile energy-gain spectra for soft charge-transfer collisions and compare them with recent experimental results by Selberg *et al.* [6]. A short discussion and a comparison of the present critical radii and energy defects with those of a simple classical barrier estimate for a conducting sphere [4,8] are also given.

Interactions between slow highly charged projectile ions and complex neutral targets may lead to the capture of several electrons into highly excited projectile states. In many cases the main features of the collision dynamics are well represented within a classical over-barrier model (COBM). Different versions of such models have been developed and applied to a variety of collision systems, such as ion-atom [9–11], ion-cluster [12–14,8,15], and ion-surface collisions [16–19]. The basic feature in all these models is the treatment of charge transfer as the classically allowed sequential transition of electrons over an internuclear potential barrier. This barrier is located between the projectile and the target and the active electron is transferred between the lowest Stark-shifted resonant states above this barrier. In contrast to the quasistatic models used for ion-atom collisions (and their direct generalizations [8,19]), the present model follows the one developed in Ref. [16] for ion-surface collisions in that the dynamics of the heavy particles as well as the flow of the electrons are treated by time-dependent equations. In particu-

lar, the electronic charge is treated as a continuous variable satisfying a set of rate equations and charge exchange is modeled as a continuous classical current of (nondiscretized) negative charge between target and projectile.

During charge-state-changing collisions, the energy defect Q is manifested in two different ways, which we will illustrate here for the simple case of a more than singly charged projectile incident on a quasi-one-electron target. We assume that at a certain distance on the incoming trajectory the electron is captured out of a Stark-shifted state into an energetically resonant projectile state. As the projectile moves on, the captured electron is influenced by the now charged target in such a way that its energetic upward shift on the outgoing trajectory is smaller than the downward shift it experienced before capture on the incoming trajectory. This asymmetry in level shifts results in a stronger binding of the electron after the collision compared to its initial binding to the target and the difference between the (negative) electronic binding energies before and after the collision is per definition equal to the positive-energy defect Q. The corresponding decrease in electronic potential energy of the collision system is balanced by an increase in the translational kinetic energy, which, for soft collisions between light projectiles and heavy targets, primarily results in a gain of kinetic energy of the projectile [20]. Equivalently, projectile energy gain can be explained by integrating the dynamically varying force between target and projectile along the trajectory. This force changes asymmetrically for the incident and outgoing trajectory. Apart from polarization interactions, the potential strength of the prevailing Coulomb interaction changes from zero (before capture) to one (after capture) and results in a difference of work done on the incident and outgoing trajectory. This difference, the net kinetic energy gain of the projectile and target, equals the energy defect Q. Under conditions (as above and as applicable in this work) where the recoil energy of the heavy target can be neglected, Q mainly manifests itself experimentally as a projectile energy gain.

So far, the dynamical COBM has been successfully applied to soft collisions between highly charged ions and C_{60} and provided a variety of observables, such as final charge

state distributions, capture cross sections, and projectile deflection angles [12–15,21]. Our main goal in this work is to present extensions to this model that allow for the simulation of the main features in recently measured, projectile, kinetic-energy gain spectra [6]. In Sec. II we give a brief summary of the dynamical COM [16,12–15] (Sec. II A) and describe in more detail the calculation of energy defects Q, both as differences in electronic binding energies and by integration of the force along the trajectory (Sec. II B). In Sec. III we discuss the simulated energy-gain spectra for $3.3q$-keV Ar^{q+}, $q=8,13,14,15$, colliding with C_{60} in comparison with recent high-resolution measurements [6]. In particular we compare the present theoretical results for the energy defects Q as functions of the numbers of removed target electrons with the corresponding experimental quantities and with a simpler classical barrier estimate for a conducting sphere. Our simulated Q values and absolute total and energy-gain differential cross sections are in fair agreement with experimental results for the removal of up to five electrons from C_{60}. Section IV contains our conclusions. Unless otherwise stated, we shall use atomic units throughout this work.

II. THEORY

A. Summary of the dynamical classical over-barrier model

In this subsection, we briefly outline the dynamical COBM for soft ion-cluster collisions. For a detailed description of this model, we refer to an earlier publication [12].

During the ion-cluster interaction, energy levels, level occupations, transition rates, and total charges of target and projectile vary as a function of R, the distance between the centers of mass of target and projectile. For the slow collisions considered in this work ($v \sim 0.2$), it can be assumed that R does not change on the time scale of resonant electronic transitions and an adiabatic approximation is generally justified.

In order to be captured or recaptured, the active electron is required to overcome the potential barrier V_B between target and projectile that is formed by the total electronic potential

$$V(q_p,q_t,R,z) = -\frac{q_p}{|R-z|} - \frac{q_t}{z} + V_{im}(q_p,R,z), \quad (2.1)$$

where q_p and q_t are the charges of projectile and target acting on the electron in transition. The electron coordinate along the "internuclear axis" is denoted by z. The image potential V_{im} includes the active electron's interaction with its self-image and with the image of the effective projectile charge q_p in the target.

As the projectile approaches the target, the first resonant transfer of an electron becomes possible at the distance R_1^*, when V_B energetically moves below the highest occupied target level. Similarly, as R decreases, a second, third, etc., electron may be captured at critical distances $R_2^* > R_3^* \cdots$ on the incoming trajectory. Since the electronic charge is treated as a continuous parameter, some assumption has to be made as to when a complete electron has been transferred. In practice, the critical over-barrier distances are extracted from the calculated impact-parameter-dependent final charge states of the target in the following way: We assume a straight-line

trajectory for the projectile and let R_1^* denote the impact parameter at which charge begins to flow from the target to the projectile. R_2^* is then the impact parameter at which one unit of charge has left the target, etc. We relate critical distances to geometrical cross sections for the production of specific charge states $i+$ of C_{60},

$$\sigma_i = \pi[(R_i^*)^2 - (R_{i+1}^*)^2], \quad (2.2)$$

and to the total geometrical cross section $\sigma_{tot} = \pi(R_1^*)^2$.

We describe the projectile within an independent-electron approach based on hydrogenic shells n with energy levels, occupation numbers, and degeneracies denoted by $\epsilon_n^p(R)$, $a_n(R)$, and $A_n = 2n^2$. We do not resolve angular-momentum sublevels. During the collision, the projectile energy levels shift due to image-charge effects, Stark shifts induced by a charged target, and the dynamical change in screening induced by varying level populations. Target energy levels $\epsilon_m^t(R)$ are Stark shifted downward in the electric field of the positive projectile. After the capture of target electrons, positive charge accumulates on the target, which results in an additional downward shift of the target and projectile spectra.

As described in detail in [12], the time evolution of the occupations $a_n(t)$ and $b_m(t)$ of projectile shells n and target levels m are obtained by integrating classical rate equations of the form

$$\frac{d}{dt}a_n = \Gamma_{RN} - \Gamma_{RL}\,a_n + \sum_{n'>n}\Gamma_{n',n} - 2\sum_{n'<n}\Gamma_{n,n'}, \quad (2.3)$$

$$\frac{d}{dt}b_m = \Gamma_{RL} - \Gamma_{RN}, \quad (2.4)$$

for the known initial occupations of projectile and target a_n^0 and b_m^0. Analytical expressions for the resonant-capture rates Γ_{RN} and resonant-loss rates Γ_{RL} are derived in Ref. [12] as classical negative transfer currents. All rates and occupation numbers implicitly depend on $R(t)$ and Eqs. (2.3) and (2.4) are solved simultaneously with Newton's equation for the projectile motion. In the two last terms of Eq. (2.3) we only include fast Auger transitions for which the two active electrons start in the same shell and that partly relax a multiply excited projectile while competing resonant electron transfer occurs. We model these fast transitions according to [16] and include statistical weights in the Auger transition rates Γ_{n_1,n_2} to take into account the number of electrons in the initial and final active shells. For a more detailed discussion of the Auger transition rates we refer to Refs. [15] and [16]. Slow Auger relaxation channels are not included as they can be neglected *during* the collision. These slow transitions have a very small influence on the translational kinetic energy since the emission of mostly slow electrons results in small and isotropic momentum transfers to the recoiling projectile. Further downstream, when resonant transfer processes are classically forbidden, Auger processes start to determine the final charge state of the projectile. Downstream Auger and radiative relaxation steps can be accounted for by enhancing the dynamical COBM with a simple relaxation scheme [15].

The dynamical COBM is usually limited to impact parameters larger than a certain minimal value b_{min} for which collision-induced fragmentation of the target can be excluded. However, the COBM can obviously be extended to impact parameters that result in capture-induced fragmentation if the corresponding fragmentation time scale is large compared to the collision time. An estimate for b_{min} is thus given by the onset for the production of target charge states that lead to fragmentation during the collision.

In order to determine the ground-state electronic structure of C_{60} and its positive ions C_{60}^{i+} with $i \leq 7$, we use the results of a self-consistent Dirac-Fock-Slater (DFS) calculation similar to the one reported in [14]. This electronic structure calculation is based on a molecular-orbital linear combination of atomic orbitals expansion scheme, which uses the $2s$, $2p_{1/2}$, and $2p_{3/2}$ atomic orbitals of C and bond distances of 2.772 and 2.561 between the C atoms, corresponding to the radius $a = 6.681$ of the buckminster fullerene. It yields the DFS single-particle energies of C_{60}^{i+} for $i = 0, \ldots, 7$ and the sequence of ionization potentials $I_{i=1,\ldots,7} = 7.24$, 10.63, 14.01, 17.44, 20.78, 24.24, and 27.54 eV, in good agreement with other calculated and experimental data ([14] and references therein). Higher ionization potentials I_i, $i > 7$, can be approximated by taking into account the work necessary to remove an eighth, etc., electron from the surface of a conducting sphere of radius a, $I_i = I_1 + (i-1)/a$ [12].

The present version of the classical over-barrier model [12,13] approximates the target response to the external charges of active electrons and projectile ion by classical image potentials of a conducting sphere [4,12,8,15]. The use of a conducting sphere as a model of C_{60} has been questioned [6,8,22] since such a model does not allow the positive charges on the fullerene surface to be localized. We plan to study the inclusion of such effects in the future. However, since the major contribution to the projectile kinetic-energy gain is accumulated at large ion-C_{60} separations, these effects are of minor importance for the interactions with highly charged ions considered in this work.

B. Simulation of projectile energy-gain spectra

The change in the balance between the potential and the kinetic energy of the collision system can be obtained by integrating the net force between the target and projectile along the trajectory. In the center-of-mass frame of reference this amounts to integrating the force that governs the motion of the projectile of reduced mass along its trajectory. For convenience we call the so-obtained quantity the ''nuclear'' energy defect Q_{nuc} since it directly refers to the motion of the reduced-mass projectile considered as a structureless particle of variable charge. The net force is the sum of the direct Coulomb and image charge interactions between target and projectile and is provided as a function of time within our dynamical over-barrier model.

Due to energy conservation, Q_{nuc} is identical to the difference of total electronic binding energy of the collision system before and after the collision. We shall use the symbol Q_{el} to denote this as ''electronic'' energy defect. Since our simulation includes approximations to the complex dynamics of the multiparticle collision system that affect in
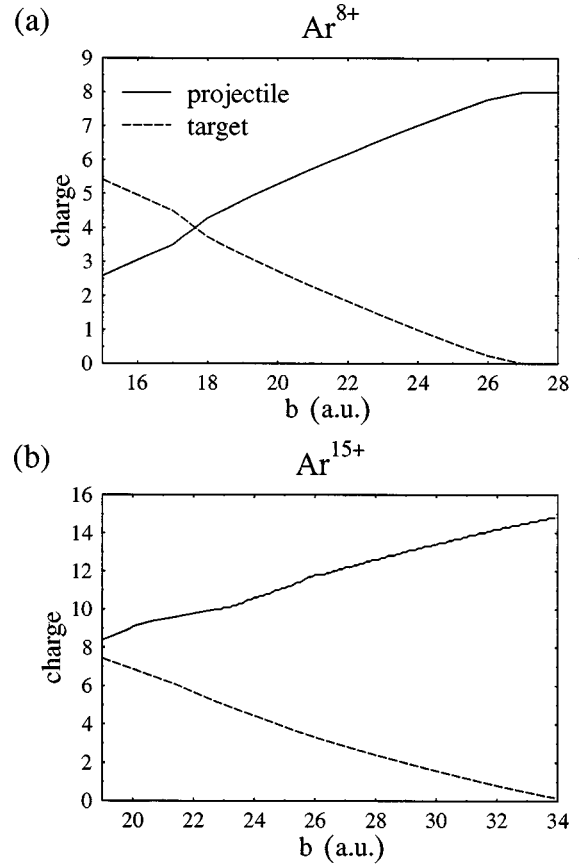

FIG. 1. Distribution of target and projectile charge states as a function of the impact parameter b for collisions of 3.3q-keV Ar^{q+} ions with C_{60}. The projectiles are relaxed with respect to the fast Auger transition explicitly included in the rate equations. (a) $q = 8$ and (b) $q = 15$.

particular the coupling between nuclear and electronic degrees of freedom, we expect our calculated values for Q_{el} and Q_{nuc} to differ. The difference $|Q_{nuc} - Q_{el}|$ is thus related to the accuracy of our simulation of the translational energy gains.

We calculate the target and projectile contributions for trajectories with impact parameter b to the total electronic energy defect $Q_{el}(b)$ as follows. For the projectile, we include the occupation-weighted energy changes of all active shells (neglecting those of inactive lower shells; cf. the discussion on screening below),

$$Q_{el}^{projectile}(b) = \sum_{n, \Delta a_n(b) \neq 0} [a_n(t_i)\epsilon_n^p(t_i) - a_n(t_f)\epsilon_n^p(t_f)].$$

$$(2.5)$$

The times t_i and t_f are long before and long after the collision. The (noninteger) impact-parameter-dependent final shell occupations $a_n(t_f)$ are relaxed with respect to the ''fast'' Auger relaxation steps included in the COBM. Since the emission of Auger electrons changes the projectile energy gain only by a small amount (due to the small ratio of electron to projectile mass), we do not need to include long-range relaxation steps that would fully relax the projectile. The occupation change of projectile shell n is given by

$\Delta a_n(b) = a_n(b,t_f) - a_n(b,t_i)$. Screening on the projectile is treated by assuming full screening by inner and no screening by outer and equivalent electrons.

With respect to the target, we first determine the amount of captured charge $q_t(t_f) - q_t(t_i)$ and then take the nearest lower integer charge $n_t(t_f)$. For our case of an initially neutral target, the captured charge amounts to the final target charge $q_t(t_f)$. The target contribution to the electronic energy defect is now obtained from the sequence of (positive) ionization potentials I_i, $i = 1,2,3,\ldots$, according to

$$Q_{el}^{target}(b) = \begin{cases} -q_t(t_f)I_1 & \text{if } q_t(t_f) \leq 1 \\ -\sum_{i=1}^{n_t(t_f)} I_i - [q_t(t_f) - n_t(t_f)]I_{n_t(t_f)+1} & \text{if } q_t(t_f) > 1. \end{cases} \quad (2.6)$$

The total electronic energy defect is then given by

$$Q_{el}(b) = Q_{el}^{target}(b) + Q_{el}^{projectile}(b). \quad (2.7)$$

In order to compare our theoretical data with measured projectile energy-gain spectra, we first relate the critical radii for the sequential capture of electrons to (nuclear or electronic) energy defect values and to the number of electrons that are captured for a particular impact parameter. For impact parameters $b_i = R_{i+1}^*$, i electrons have been captured and the corresponding energy defects Q_i are $Q_{nuc}(b_i)$ and $Q_{el}(b_i)$. The simulated energy-gain spectra are given by the sequence of infinitely narrow peaks

$$\frac{d\sigma^{theory}}{d\Delta E} = \sum_i \sigma_i \delta(\Delta E - Q_i). \quad (2.8)$$

In order to relate this expression to the intensities in measured projectile energy-gain spectra, we fold it with a Gaussian distribution

$$R(\Delta E - \Delta E') = \sqrt{\frac{4 \ln 2}{\pi \Delta Q^2}} \exp\left\{ -4 \ln 2 \left(\frac{\Delta E - \Delta E'}{\Delta Q} \right)^2 \right\}, \quad (2.9)$$

the full width at half maximum of which ΔQ is given by the (energy- and charge-state-dependent) resolution of the experiment. By convoluting Eq. (2.8) with Eq. (2.9), we obtained the simulated energy-gain spectrum, corrected for the finite experimental energy resolution

$$\frac{d\sigma}{d\Delta E} = \sum_i \sigma_i R(\Delta E - Q_i). \quad (2.10)$$

This method allows for the interpretation of peaks in the measured spectra in terms of the corresponding number of captured electrons. In conjunction with the simulated projectile occupation changes $\Delta a_n(b_i)$ it also allows for the assignment of final projectile shells into which capture occurs at particular energy gains. We note that we may neglect the small difference between the net and the projectile kinetic-energy gain for these large-impact parameter collisions (and hence equate energy defects with projectile kinetic-energy gains) due to the large mass and relatively small recoil energy of the C_{60} target.

III. NUMERICAL RESULTS AND DISCUSSION

Figure 1 shows the simulated projectile and target charge states as a function of impact parameter b for collisions of 3.3q-keV Ar^{q+}, $q = 8,15$, ions with C_{60}. The sequence of critical radii R_i^* for the capture of i electrons can be extracted from the impact-parameter dependence of the final

TABLE I. Critical over-barrier radii R_i^* (in a.u.) for the production of final target charge states $i+$ in 3.3q-keV Ar^{q+}, $q = 8,13,14,15$, on C_{60} collisions.

i	Ar^{8+}	Ar^{13+}	Ar^{14+}	Ar^{15+}
1	26.9	32.8	33.8	34.8
2	23.9	29.5	30.5	31.4
3	21.6	27.1	28.0	28.9
4	19.4	24.8	25.7	26.7
5	17.7	23.0	23.9	24.8
6	15.9	21.2	22.1	23.0

TABLE II. Geometrical cross sections σ_i (in 10^{-15} cm^2) for the production of final target charge states $i+$ in 3.3q-keV Ar^{q+}, $q = 8,13,14,15$, on C_{60} collisions. σ_{tot} is the calculated total cross section for charge-state changing collisions. σ_{tot}^{expt} are measured cross sections [6,4]. The projectile shell n into which capture occurs for a particular charge state q is given in parentheses. In case two shells are listed for the same q and i, the larger contribution comes from the shell listed first.

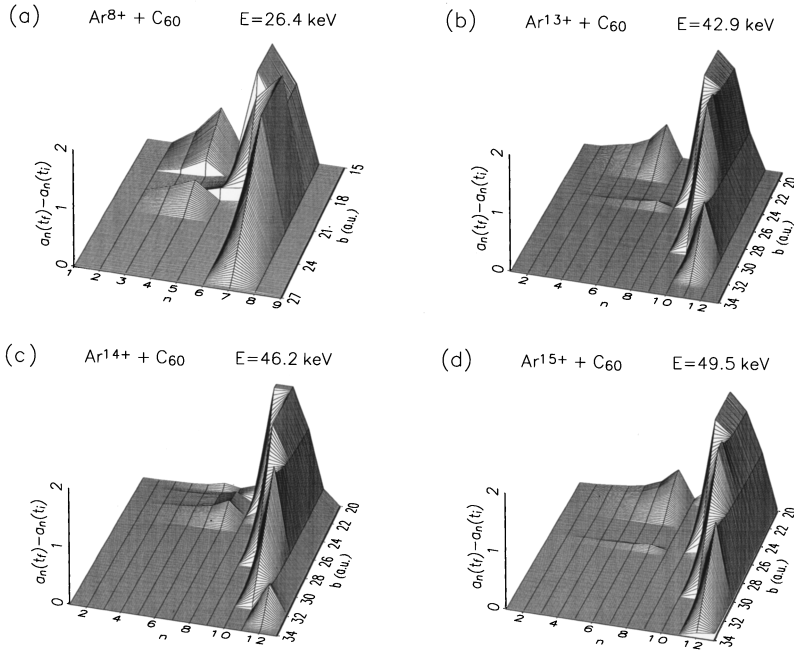| Cross section	Ar^{8+}	Ar^{13+}	Ar^{14+}	Ar^{15+}
σ_1 (n)	13.4 (7)	18.1 (11)	18.7 (12,11)	19.8 (12,13)
σ_2 (n)	9.2 (7)	11.9 (10)	12.9 (11)	13.3 (12,11)
σ_3 (n)	7.9 (7,6)	10.5 (10,9)	10.9 (10)	10.8 (11)
σ_4 (n)	5.6 (6)	7.6 (9)	7.9 (10)	8.6 (10,11)
σ_5 (n)	5.3 (6)	7.0 (9)	7.3 (9)	7.6 (10)
σ_{tot}	63.7	94.6	101	107
σ_{tot}^{expt} [a]	46±14	101±28	71±20	100±31
σ_{tot}^{expt} [b]	44±18			

[a]Reference [6].
[b]Reference [4].

FIG. 2. Changes in projectile shell occupations with respect to the initial occupations. The system and parameters are as in Fig. 1. The projectiles are relaxed with respect to the fast Auger transition explicitly included in the rate equations. (a) $q=8$, (b) $q=13$, (c) $q=14$, and (d) $q=15$.

target charge state (cf. Fig. 1) and is given in Table I. Table II contains the geometrical cross sections for the production of specific charge states $i+$ of C_{60} and the total capture cross sections derived from these critical radii. Table II also shows our calculated total cross sections to be in fair agreement with the absolute measurements performed by Selberg *et al.* [6] and Walch *et al.* [4]. As one might expect, the total cross sections increase with increasing initial charge state of the projectile. This is also true for the target charge state resolved cross sections σ_i, except for $i=3$ and incident Ar^{14+}.

The simulated changes $\Delta a_n(b)$ in the population of shell n as a function of impact parameter are shown in Fig. 2. The data in Fig. 2 give the projectile charge states given in Fig. 1. The resonantly populated shells for Ar^{8+} are $n=6$ and $n=7$ (Table II). Population changes in lower shells ($n=3,4$) are due to fast Auger transitions [Fig. 2(a)]. For the higher initial projectile charge states [Figs. 2(b)–2(d) and Table II] higher projectile shells are resonantly populated. For Ar^{13+} the highest resonantly populated shell is $n=11$, whereas for Ar^{14+} and Ar^{15+} electrons are captured in shells up to $n=12$, with larger population in the highest populated shell for the higher initial charge state (Ar^{15+}). Population changes below $n=8$ in Figs. 2(b)–2(d) are due fast Auger transitions. Our simulated results are in good overall agreement with the experimental results of Selberg *et al.* [6], who measured single-electron capture to be dominated by capture to $n=7$, 10, 11, and 12 for $q=8$, 13, 14, and 15, respectively. Looking closer at Fig. 2, it is apparent that although $n=11$ is the outermost populated shell for Ar^{13+}, the population of $n=10$ becomes much stronger at only slightly smaller impact parameters. This may account for the assignment of $n=10$ in the experimental spectrum. There is a somewhat similar situation for $q=15$ [cf. Fig. 2(d)] and $n=12$ and $n=11$. In the experimental spectra there are actually two peaks of similar heights that were ascribed to these two quantum numbers [6].

The target contribution $Q_{el}^{target}(b)$ [Eq. (2.6)] and the con-

tribution of the projectile $Q_{el}^{projectile}(b)$ [Eq. (2.5)] to the electronic energy defect $Q_{el}(b)$ [Eq. (2.7)] are shown in Fig. 3 for $q=8$ and 15. The projectile contribution is shown at two downstream distances from the point of closest approach $R=100$ and $R=50\,000$, in order to display long-range contributions and the convergence in R. $Q_{el}^{projectile}(b)$ and $Q_{el}^{target}(b)$ increase in magnitude as the initial charge of the projectile increases. The two quantities are comparable in magnitude with the slightly larger magnitude of $Q_{el}^{projectile}(b)$ leading to *positive* energy defects $Q_{el}(b)$. Table III contains the electronic and nuclear energy defects for the capture of one to five electrons.

The electronic and nuclear energy defects $Q_{el}(b)$ [Eq. (2.7)] and $Q_{nuc}(b)$ are given in Fig. 4 as a function of impact parameter. The difference of two large numbers inherent in the calculation of $Q_{el}(b)$ and shell effects (see below) are the origin of the structure in $Q_{el}(b)$. For the larger impact parameters, the electronic and nuclear defects agree within the overall quality of our dynamical COBM.

According to our simulation, the larger the energy defect is for a particular capture event, the more electrons have been captured (Table III) previously. The only exception to this general trend is given for the electronic energy defect in the case of Ar^{13+} projectiles (third column in Table III) and is related to (nonphysical) shell effects. These shell effects are due to the energy binning and restrictions on level populations for resonant and Auger transitions within the COBM. For resonant transitions some discontinuity is introduced into our simulation due to the energy binning that relates discrete energy levels to the classically continuous energy of a transferred electron. For Auger transitions the requirement of at least two electrons in the initial shell may lead to small deviations from the general trend [12,15]. We note that the nuclear energy defect for incident Ar^{13+} (fourth column in Table III) shows the general monotonic increase in the number of captured electrons.

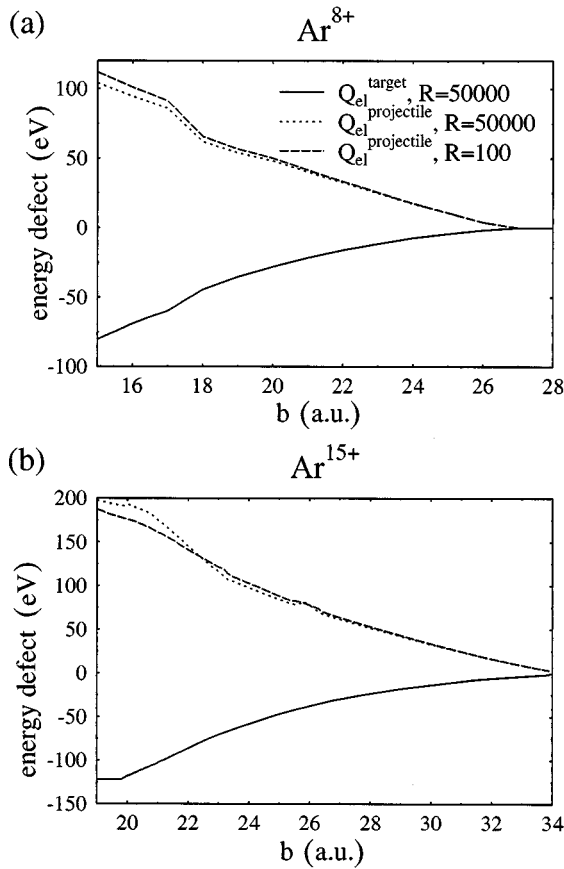In Fig. 5 we show the experimental differential energy-

FIG. 3. Electronic contributions to the energy defect. The system and parameters are as in Fig. 1. The energy defects are converged at a distance of $R_\parallel = 50\,000$ a.u. downstream. To illustrate the convergence in $R_\parallel$, the contribution of the projectile to the electronic energy defect is also shown at $R_\parallel = 100$ a.u. downstream. (a) $q = 8$ and (b) $q = 15$.

gain spectra from Selberg *et al.* [6] together with the present calculated spectra. Experimental and calculated spectra are absolute in both intensity (peak heights) and energy gain. The calculated spectra have been obtained according to Eq. (2.10) by including the experimental response function in the form of Gaussians (2.9), centered on the nuclear energy defects. The experimental widths were averaged over energy. Values for the considered incident charge states $q = 8$, 13, 14,

TABLE III. Calculated energy defects Q (in eV) for the capture of $+i$ electrons in 3.3q-keV Ar^{q+}, $q = 8,13,14,15$, collisions with C$_{60}$. Q_{el} and Q_{nuc} designate the ''electronic'' and ''nuclear'' energy defects (see the text). In an exact *ab initio* calculation Q_{el} would be equal to Q_{nuc} and the difference $|Q_{el} - Q_{nuc}|$ is indicative for the accuracy of the calculation.

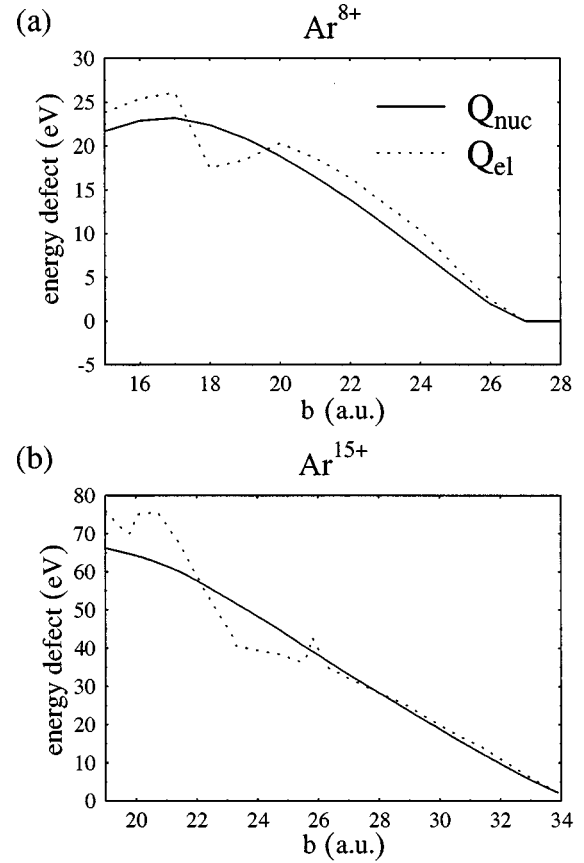|	Ar^{8+}		Ar^{13+}		Ar^{14+}		Ar^{15+}	
i	Q_{el}	Q_{nuc}	Q_{el}	Q_{nuc}	Q_{el}	Q_{nuc}	Q_{el}	Q_{nuc}
1	10.7	8.3	11.9	11.2	12.9	11.6	14.0	12.4
2	17.7	15.0	22.4	21.5	23.8	22.8	25.1	24.1
3	20.0	20.6	33.3	31.4	31.5	33.3	33.4	34.6
4	29.8	23.7	32.9	39.2	41.7	42.0	38.2	44.4
5	30.8	24.8	45.2	46.2	46.4	50.0	45.5	53.1

FIG. 4. Electronic and nuclear contributions to the energy defect, converged at a distance of $R_\parallel = 50\,000$ a.u. downstream. The system and parameters are as in Fig. 1. (a) $q = 8$ and (b) $q = 15$.

and 15 are $\Delta Q = 4.7$, 7.8, 8.9, and 9.4 eV, respectively. The areas under the simulated curves in Fig. 5 are equal to the sum of the respective calculated cross sections σ_i in Table II. The simulation curves include the three lowest-energy gains for Ar^{8+} and the five lowest-energy gains for all other incident charge states of the projectile. The measured energy-gain spectra in Ref. [6] are relative in the peak heights (intensities) and absolute in the peak positions (kinetic-energy gains). In order to put these relative intensities (peak heights) on an absolute scale indicating energy-differential kinetic-energy gains, we put the areas under the measured energy-gain curves equal to the *total* experimental cross sections of Ref. [6] (Table II). The high-energy tails of the measured energy gain spectra correspond to the capture of more than three electrons (for Ar^{8+}) or more than five electrons (Ar^{q+}, $q = 13,14,15$), i.e., to collisions with impact parameters that are smaller than those currently accessible to our COBM simulation. For the lower part of the spectrum, which yields the dominant contribution to the total cross section, we find good agreement with the measured spectra in the overall trend and very good agreement for the first energy-gain peak for incident Ar^{q+}, $q = 13,14,15$. The calculated nuclear energy defects are also indicated by arrows and correspond to capture into the projectile shells specified in Table II. Further investigations are necessary to fully understand the high-energy part of the kinetic-energy-gain spectra measured in Ref. [6].

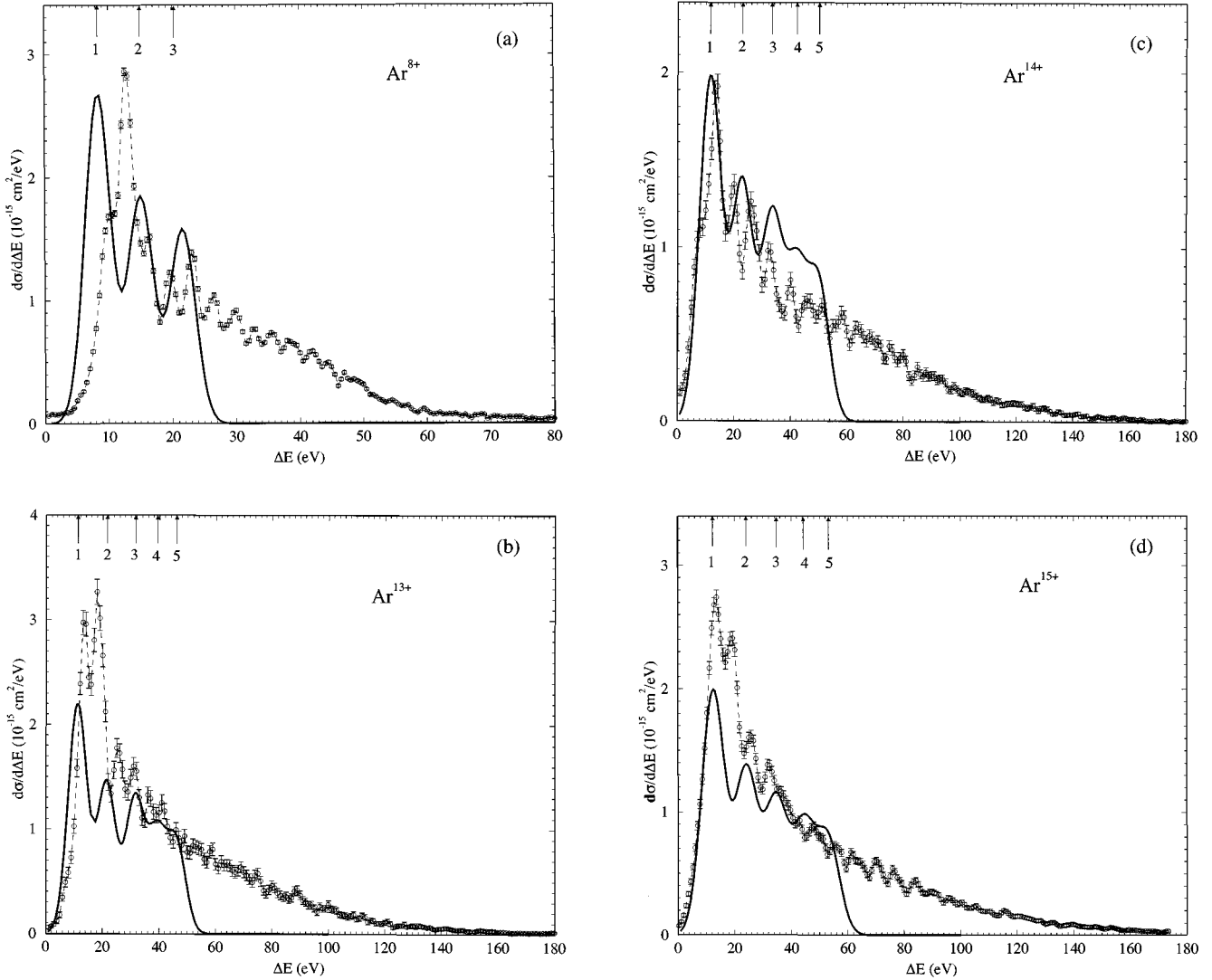As a consistency check we compared the critical radii and

FIG. 5. Simulated and measured projectile energy-gain spectra for Ar^{q+}-C_{60} collisions. The measured and calculated energy-gain values are absolute. The experimental errors in peak positions typically are ± 0.5 eV. Calculated energy gains correspond to the nuclear defects (see the text) folded with the experimental response function. The arrows point to the calculated nuclear energy defects for the capture of 1,2,3, . . . , electrons. (a) $q=8$, (b) $q=13$, (c) $q=14$, and (d) $q=15$.

energy defects for the present dynamical model with the more direct classical barrier estimates derived from a simple electrostatic model [4,8], where C_{60} is considered as a conducting sphere with radius $a=6.7$. In Table IV we show such a comparison with the more elementary model of Ref. [8] for the case of Ar^{13+} as projectiles. It is immediately clear that the critical radii in the two versions are very similar. Using the arithmetic mean value of the electronic and nuclear energy gains of the present dynamical version of the model, we see that these mean energy gains agree rather well with those of the more simple estimate.

IV. CONCLUSIONS

The dynamical classical over-barrier model has been extended to allow for the simulation and interpretation of projectile energy-gain spectra in soft collisions between highly charged ions and C_{60}. The energy defects have been calculated in two different ways: as the difference of electronic

TABLE IV. Critical over-barrier radii R_i^* (in a.u.), calculated energy defects Q (in eV) and geometrical cross sections σ_i (in 10^{-15} cm^2) for the capture of $i+$ electrons in 3.3q-keV Ar^{q+}, $q=13$, collisions with C_{60}. The table contains results calculated both with the present dynamical version of the classical over-barrier model and with the conducting sphere version of the model described in [8]. Q for the present model is the arithmetic mean value of Q_{el} and Q_{nuc}. The cross sections σ_i are calculated according to Eq. (2.2).

i	Present model			Model described in [8]		
	R_i^*	Q	σ_i	R_i^*	Q	σ_i
1	32.8	11.6	18.1	31.7	10.3	14.1
2	29.5	22.0	11.9	29.1	19.6	11.2
3	27.1	32.4	10.5	26.8	27.7	7.3
4	24.8	36.0	7.6	24.7	34.4	7.2
5	23.0	45.7	7.0	23.0	39.1	6.6

binding energies and by integration of the dynamically varying force between the collision partners along the trajectory, thereby allowing for an intrinsic test of the theory. In comparison with recent experiments, we find in all cases good agreement in the overall trend for the low-energy part of the energy-gain spectra, while the high-energy parts remain unexplained. In general we find good quantitative agreement with respect to peak positions (energy gains) and peak heights (intensities). This agreement between simulated and measured spectra is particularly good for the higher projectile charges considered. With the help of our simulated energy-gain spectra we have analyzed measured spectra with respect to details of the charge-transfer dynamics, such as the correlation between numbers of transferred electrons, projectile shell populations, and energy gain.

The present dynamical model does not account for the experimental finding of an appreciable cross section for high projectile energy gain. Future experiments that combine precision measurements of projectile energy gains with a recoil charge state coincidence detection may provide a more subtle test of theory. This might allow us to further fine-tune and improve the dynamical COBM and to better understand the rich structure found experimentally in highly resolved energy-gain spectra.

---

[1] W. Krätschmer, L. D. Lamb, K. Fostiropoulos, and D. R. Huffman, Nature (London) **347**, 354 (1990).

[2] D. C. Lorents, Comments At. Mol. Phys. (to be published).

[3] T. LeBrun, H. G. Berry, S. Cheng, R. W. Dunford, H. Esbensen, D. S. Gemmel, and E. P. Kanter, Phys. Rev. Lett. **72**, 3965 (1994).

[4] B. Walch, C. L. Cocke, R. Voelpel, and E. Salzborn, Phys. Rev. Lett. **72**, 1439 (1994).

[5] J. Jin, H. Khemliche, M. H. Prior, and Z. Xie, Phys. Rev. A **53**, 615 (1996).

[6] N. Selberg, A. Bárány, C. Biedermann, C. J. Setterlind, H. Cederquist, A. Langereis, M. O. Larsson, A. Wännström, and P. Hvelplund, Phys. Rev. A **53**, 874 (1996).

[7] J. P. Briand, L. de Billy, J. Jin, H. Khemliche, M. H. Prior, Z. Xie, M. Nectoux, and D. Schneider, Phys. Rev. A **53**, R2925 (1996).

[8] A. Bárány and C. J. Setterlind, Nucl. Instrum. Methods Phys. Res. B **98**, 184 (1995).

[9] A. Bárány, G. Astner, H. Cederquist, H. Danared, S. Huldt, P. Hvelplund, A. Johnson, H. Knudsen, L. Liljeby, and K.-G. Rensfeld, Nucl. Instrum. Methods Phys. Res. B **23**, 4293 (1990).

[10] A. Niehaus, J. Phys. B **19**, 2925 (1986).

[11] L. Guillemot, P. Roncin, M. N. Gaboriaud, H. Laurent, and M. Barat, J. Phys. B **23**, 4293 (1990).

[12] U. Thumm, J. Phys. B **27**, 3515 (1994).

[13] U. Thumm, J. Phys. B **28**, 91 (1995).

[14] U. Thumm, T. Baştuğ, and B. Fricke, Phys. Rev. A **52**, 2955 (1995).

[15] U. Thumm, Phys. Rev. A **55**, 479 (1997).

[16] J. Burgdörfer, P. Lerner, and F. W. Meyer, Phys. Rev. A **44**, 5674 (1991).

[17] J. Burgdörfer, in *Review of Fundamental Processes and Applications of Atoms and Ions*, edited by C. D. Lin (World Scientific, Singapore, 1993), p. 517.

[18] J. Burgdörfer, C. Reinhold, and F. W. Meyer, Nucl. Instrum. Methods Phys. Res. B **98**, 415 (1995).

[19] A. Bárány and C.J. Setterlind, Heavy Ion Phys. **1**, 115 (1995).

[20] J. Appell, in *Collision Spectroscopy*, edited by R. G. Cooks (Plenum, New York, 1978), p. 227.

[21] B. Walch, U. Thumm, M. Stöckli, and C. L. Cocke (unpublished).

[22] H. Shen, P. Hvelplund, D. Mathur, A. Bárány, H. Cederquist, N. Selberg, and D. C. Lorents, Phys. Rev. A **52**, 3847 (1995).